Received: 3 August 2019 | Revised: 27 June 2020 | Accepted: 2 August 2020

DOI: 10.1002/fld.4904

RESEARCH ARTICLE

WILEY

A centrifugal buoyancy formulation for Boussinesq-type natural convection flows applied to the annulus cavity problem

Peyman Mayeli | **Gregory J. Sheard**

The Sheard Lab, Department of Mechanical and Aerospace Engineering, Monash University, Melbourne, Victoria, Australia

Correspondence
Peyman Mayeli, The Sheard Lab, Department of Mechanical and Aerospace Engineering, Monash University, Melbourne, VIC 3800, Australia.
Email: peyman.mayeli@monash.edu

Funding information
Australian Research Council, Grant/Award Numbers: DP180102647, DP150102920

Summary

Traditionally, the Boussinesq approximation is adopted for numerical simulation of natural convection phenomena where density variations are supposed negligible except through the gravity term of the momentum equation. In this study, a recently developed formulation based on a Boussinesq approximation is presented in which the density variations are also considered in the advection terms. Extending density-variations to the advection terms captures centrifugal effects arising from both bulk enclosure rotation and within individual vortices, and thus more accurate results are expected. In this respect, the results of the proposed formulation are compared against the conventional Boussinesq simulations and weakly compressible approximation in the concentric horizontal annulus cavity. A new relation is established which maps the magnitude of the non-Boussinesq parameter of incompressible flow to the corresponding relative temperature difference of a compressible flow simulation which is in agreement with the maximum allowed Gay-Lussac number to avoid unphysical density values. For comparison purposes, variations of different thermo-fluid parameters including average and local Nusselt number, entropy generation, and skin friction up to $Ra = 10^5$ are computed. Results obtained under the proposed approximation agree with the classical Boussinesq approximation up to $Ra = 10^3$ for large non-Boussinesq parameter corresponding to the large relative temperature difference, but at $Ra = 10^5$, computed thermo-fluid parameters via the two approaches are not identical which justifies the inclusion of large Gay-Lussac number for convection dominated regime in natural convection problems.

KEYWORDS

annulus cavity, Boussinesq approximation, control volume finite-element method, Gay-Lussac, non-Boussinesq approximation, weakly compressible

1 | INTRODUCTION

Numerical simulation of natural convection phenomena, due to their many scientific and technical applications such as solar collectors, foundry devices, geophysical and astrophysical processes, and so on,[1-5] has attracted attention of researchers over several decades. Predicting the exact behavior of such systems when natural convection is the dominant

heat transfer mechanism is of paramount importance. Typically, the Boussinesq approximation (ie, ignoring density variations except in the gravity term of the momentum equation[6]) is adopted for numerical simulation of natural convection problems. In this approach, a linear state equation is typically adopted to relate density and temperature variations via a volumetric thermal expansion coefficient.

The horizontal annulus cavity is a widely used benchmark problem in numerical heat transfer research. At low Rayleigh (Ra) numbers, diffusion is the dominant mechanism, but at higher Rayleigh numbers convection ultimately dominates the heat transfer, resulting in thin boundary layers. One of the initial works in this area was performed by Thomas and Davis,[7] while Kuhen and Goldstein[8] studied natural convection in an annulus cavity by means of both experimental and numerical simulations. Sheremet and Pop[9,10] studied this problem in the context of porous media and nanofluids. The problem has been solved by a variety of numerical methods, including finite difference,[8] finite volume,[11,12] control volume finite-element,[13,14] lattice Boltzmann,[15] and finite-element based approaches such as local Petrov-Galerkin,[16,17] Galerkin radial-basis-function,[18] differential quadrature method,[19] strongly implicit procedure,[20] and so on. Studies have shown the flow to be steady state up to at least $Ra = 10^5$[12-16] across Prandtl numbers spanning air and water.

In all of the aforementioned works, the Boussinesq approximation along with a linear relation between density and temperature variations has been adopted. This is based on the assumption that the density variations are small, confining their effect to the buoyancy term. This allows the flow field to be treated as incompressible. Note that in different situations, where the density variations under the influence of the temperature non-uniformities are significant, the classical Boussinesq approximation may produce inaccurate results. Available remedies to overcome this issue in the literature may be divided into two major categories. The first remedy is compressible solution of the governing equations. This approach was used by Vierendeels et al[21] and Becker and Braack[22] for numerical simulation of the natural convection problem at low Mach number. The second remedy is dealing with the incompressible Navier-Stokes equations accompanying with some modifications to achieve more accurate results. One approach in this category is to include the linear state relation between density and temperature to terms beyond only the gravity term, which results in the emergence of the Gay-Lussac number ($Ga = \beta\Delta\theta$) in the governing equations. This parameter describes the level of density variations caused by the temperature field. It can be shown that the Boussinesq approximation is retrieved as the Gay-Lussac number goes to zero.[23] For this approach, the difference between the Boussinesq approximation and considering the Gay-Lussac number for the Rayleigh number regime that leads to a steady state solution of the problem, was studied by Szewc et al[23] for a rectangular cavity filled with air. They reported a 4% discrepancy of the average Nusselt number between the two approaches. Lopez et al[24] described an alternative approach, for the treatment of rapidly rotating flows, whereby buoyancy effects were extended to the centrifugal part of the advection term to capture centrifugal effects in those flows.

In the context of experimental studies, some works have considered non-Boussinesq effects. These studies often emphasize the properties of the working fluid (often a liquid), and especially its viscosity that is sensitive to temperature variations. The Boussinesq approximation is developed based on small density variations assumption which implies a small temperature difference. For liquid working fluid cases, having large temperature differences between hot and cold surfaces and its effect on the viscosity along with applying the Boussinesq approximation for non-gaseous mixtures may result in inaccurate results. For instance, Valori et al[25] used water and methanol as their working fluid beyond the validity of the Boussinesq approximation in a cubical Rayleigh-Bénard convection cell. They found that the non-Boussinesq effect manifests itself as an increase of time-averaged horizontal velocity component close to the bottom wall of the cell and as a global top-bottom asymmetry of the velocity field. In another study, Manga and Weerante[26] used corn syrup as working fluid in their experimental set-up at high Prandtl and Rayleigh numbers ($10^3 \leq Pr \leq 10^6$, $10^4 \leq Ra \leq 10^8$). Corn syrup exhibits a strict viscosity dependence on temperature. They found that at their largest Rayleigh number, $Ra = 10^8$, the Nusselt number (Nu) was lower than expected, based on an extrapolation of the Nu- Ra relationship determined at lower Rayleigh numbers. A similar experimental study was also performed by Zhang et al[27] in which glycerol was used as working fluid in a square cubic cell at higher Rayleigh numbers ($10^6 \leq Ra \leq 10^9$) and lower Prandtl numbers ($10^2 \leq Pr \leq 10^3$). They presented a simplified 2-D model for the mean centre temperature based on an equation for the thermal boundary layer and compared that with the experimental results.

The idea of applying variable properties as a separate class of non-Boussinesq approximation is continued in numerical simulations as well. For example, Zhang and Cao[28] investigated the non-Boussinesq effects of natural convection in a horizontal annulus with aspect ratio of 2.0 over $10^4 \leq Ra \leq 10^6$. They reported discrepancies among obtained solutions via different approaches of variable property-based lattice Boltzmann flux solver method as an influence of the non-Boussinesq effect that is induced by partial or total variations in fluid properties on the flow instability behaviors and heat transfer characteristics.

In the present study, the work of Lopez et al[24] informs the presentation of a new form of the governing equations based on the idea of considering density variations through both the advection term (capturing centrifugal effects) as well as the gravitational term in the momentum equations for natural convection problems. This formulation is implemented into a control volume finite-element method solver and results are investigated for local and average Nusselt number, entropy generation and skin friction in a horizontal concentric annulus cavity up to $Ra = 10^5$. The rest of the article is organized as follows: Section 2 presents the aforementioned formulation, Section 3 introduces the geometry of the problem and details numerical treatment including accuracy and mesh dependency. In Section 4, the mismatch between Boussinesq and non-Boussinesq approximations is scrutinized, and conclusions are drawn in Section 5.

2 | GOVERNING EQUATIONS AND PARAMETERS

Under the classical Boussinesq approximation for buoyancy, density differences are neglected except with respect to the gravity term, but as mentioned before, one approach to extend beyond the Boussinesq approximation is elaborated in Lopez et al,[24] in which the density variations are considered through the advection terms as well as the buoyancy term. In Lopez et al,[24] the density $\rho = \rho_0 + \rho'$ comprises a constant (ρ_0) and a perturbation part (ρ') that captures the temperature dependences, density variations due to fluid density stratification or density variations in a binary fluid with miscible species of different densities, and so on. This extension produces the modified governing momentum equation in the inertial frame for a Newtonian fluid,

$$\rho_0(\partial_t + u \cdot \nabla)\boldsymbol{u} = -\nabla p^* + \mu\nabla^2\boldsymbol{u} + \rho\boldsymbol{f} - \rho'\nabla\phi - \rho'(\boldsymbol{u} \cdot \nabla)\boldsymbol{u}. \tag{1}$$

Here a modified pressure is introduced as $p^* = p + \rho_0\phi$, where ϕ is the gravitational potential whose gradient opposes the gravitational acceleration vector, that is, . $\nabla\phi = -g\boldsymbol{e}_g$, where $\boldsymbol{e}_g$ is the unit vector in the direction of gravity. In addition, the term $\rho\boldsymbol{f}$ in Equation (1) accounts for additional body forces that may act on the fluid, but this is taken as zero throughout this study. Here buoyancy effects are also considered with respect to the advection term, but a unified density is used to derive the governing equations under the proposed approximation. Starting with the steady-state incompressible momentum equation in vector form,

$$\rho(\boldsymbol{u} \cdot \nabla)\boldsymbol{u} = -\nabla p + \mu\nabla^2\boldsymbol{u} + \rho g\boldsymbol{e}_g, \tag{2}$$

and dividing Equation (2) by the reference density, ρ_0, yields

$$\frac{\rho}{\rho_0}(\boldsymbol{u} \cdot \nabla)\boldsymbol{u} = -\frac{1}{\rho_0}\nabla p + \nu\nabla^2\boldsymbol{u} + \frac{\rho}{\rho_0}g\,\boldsymbol{e}_g. \tag{3}$$

Following the Boussinesq approach, only the first term of the density state relation is taken into account. Substituting the density state relation $\rho/\rho_0 = 1 - \beta\theta$ and the modified pressure into (3) yields

$$(\boldsymbol{u} \cdot \nabla)\boldsymbol{u} = -\frac{1}{\rho_0}\nabla p^* + \nu\nabla^2\boldsymbol{u} - \beta\theta g\boldsymbol{e}_g + \beta\theta(\boldsymbol{u} \cdot \nabla)\boldsymbol{u}. \tag{4}$$

Using dimensionless quantities

$$X = \frac{x}{L}, Y = \frac{y}{L}, U = \frac{uL}{\alpha}, P = \frac{p^*L^2}{\rho\alpha^2}, \Theta = \frac{\theta}{\Delta\theta} = \frac{T - T_0}{T_h - T_c}, \tag{5}$$

one can derive the dimensionless form of the momentum equation for natural convection problems,

$$(\boldsymbol{U} \cdot \nabla)\boldsymbol{U} = -\nabla P + Pr\nabla^2\boldsymbol{U} - RaPr\Theta\boldsymbol{e}_g + Ga\Theta(\boldsymbol{U} \cdot \nabla)\boldsymbol{U}. \tag{6}$$

Equation (6) introduces the Prandtl number $Pr = \nu/\alpha$ characterising the ratio of the molecular to thermal dissipation, and the Rayleigh number $Ra = g\beta\Delta\theta{L_{\text{ref}}}^3/\nu\alpha$ characterising the ratio of buoyancy to viscous and thermal dissipation. It also reveals the Gay-Lussac number ($Ga = \beta\Delta\theta$) in the last term on the right-hand side. We restrict ourselves to modest values of Ga to avoid unphysical (negative) density under the linear density-temperature state relation. The linear density-temperature state relation in terms of dimensionless temperature and Gay-Lussac number is expressed as

$$\frac{\rho}{\rho_0} = 1 - \beta\theta = 1 - \beta\Delta\theta\Theta = 1 - Ga\Theta. \tag{7}$$

Regarding the highest dimensionless temperature in the physical domain ($\Theta_h = 0.5$), the constraint $Ga < 2$, guaranties a physical value for density. Introduction of a Froude number characterising the ratio of inertia to gravity,

$$Fr = \frac{U_{ref}^2}{gL} = \frac{(\alpha/L)^2}{gL} = \frac{\alpha^2}{gL^3},$$

permits the Gay—Lussac parameter to be expressed as $Ga = \beta\Delta\theta = FrRaPr$, and thus

$$Fr = \frac{Ga}{RaPr}, \tag{8}$$

which has a maximum value of

$$Fr_{max} = \frac{2}{RaPr} \tag{9}$$

at each given Rayleigh and Prandtl number. Using Equation (8), Equation (6) becomes

$$(\boldsymbol{U}\cdot\nabla)\boldsymbol{U} = -\nabla P + Pr\nabla^2\boldsymbol{U} - RaPr\Theta(\boldsymbol{e}_g - Fr(\boldsymbol{U}\cdot\nabla)\boldsymbol{U}). \tag{10}$$

As can be seen, Equation (10) is consistent with the momentum equation under the Boussinesq approximation, except for the additional inertial buoyancy term on the right hand side. When expressed in this form, it is apparent that the action of this additional term is to modify the effective direction (and strength) of the gravity locally throughout the flow which is ignored in the conventional Boussinesq approximation. Indeed, regions which are experiencing higher spatial accelerations (described by $(\boldsymbol{U}\cdot\nabla)\boldsymbol{U}$) will experience deviations from the Boussinesq buoyancy approximation. The strength of these deviations relative to gravity is described by Fr, with $Fr \to 0$ (and $\beta\Delta\theta \to 0$) recovering the classical Boussinesq approximation.

The effect of Fr on the buoyancy-driven flow is investigated in Section 4. Thus, under the proposed approximation, the general form of the governing equations is expressed as

$$\begin{cases} \nabla\cdot\boldsymbol{U} = 0, \\ (\boldsymbol{U}\cdot\nabla)\boldsymbol{U} = -\nabla P + Pr\nabla^2\boldsymbol{U} - RaPr\Theta(\boldsymbol{e}_g - Fr(\boldsymbol{U}\cdot\nabla)\boldsymbol{U}), \\ (\boldsymbol{U}\cdot\nabla)\Theta = \nabla^2\Theta. \end{cases} \tag{11}$$

In this formulation, large values of Ga are not considered, which would necessitate its inclusion in other terms; instead it is shown that the effect on the flow is non-negligible through advection in certain situations, such as rapid rotation.[24] The present formulation generalizes the description of centrifugal effects both globally *and* locally, and about any axis.

For comparison, results are compared to natural convection simulations under the weakly compressible approximation.[29] In this approach, due to the small compressibility ratio (identified by Mach number) in natural convection problems, acoustic waves of the fully compressible form of the Navier-Stokes equations are filtered. This approach is also known as low Mach number scheme (LMS). Aside from filtering acoustic waves, the main feature of the LMS model is splitting the total pressure into a mechanical (local) pressure that acts in the momentum equation to balance the advection with buoyancy and diffusion, and a global thermodynamic pressure that is used to update density variations during the solution procedure. Paillere et al[30] compared results of the LMS model vs fully compressible Navier-Stokes equations for both small and large temperature differences (beyond the Boussinesq approximation) and showed that the LMS model can simulate natural convection with high fidelity and negligible differences compared to the hyperbolic compressible Navier-Stokes equations. The conservative form of the governing equations under the LMS approximation are[31]

$$\begin{cases} \frac{\partial\rho^*}{\partial t^*} + \nabla\cdot(\rho\boldsymbol{u}) = 0, \\ \frac{\partial(\rho^*\boldsymbol{u})}{\partial t^*} + \nabla\cdot(\rho^*\boldsymbol{u}\otimes\boldsymbol{u}) = -\nabla p^* + \rho^*\boldsymbol{e}_g + \nabla\cdot\boldsymbol{\tau}^*, \\ \rho^* c_p\left(\frac{\partial T}{\partial t^*} + \nabla\cdot(\boldsymbol{u}T)\right) = \kappa\nabla^2 T + \frac{\mathrm{d}p_{th}}{\mathrm{d}t}, \\ p_{th} = \rho^* RT. \end{cases} \tag{12}$$

Using the non-dimensionalizations

$$X=\frac{x}{L}, Y=\frac{y}{L}, \boldsymbol{U}=\frac{\boldsymbol{u}L}{\alpha}, P=\frac{p^{*}L^{2}}{\rho\alpha^{2}}, \Theta=\frac{T}{T_{0}}, \varepsilon=\frac{T_{h}-T_{c}}{2T_{0}}, P_{\mathrm{th}}=\frac{p_{th}}{p_{0}}, t=\frac{t^{*}L}{u}, Z=\frac{R}{R_{0}}, \rho=\frac{\rho^{*}}{\rho_{0}} \tag{13}$$

the dimensionless form of Equation (12) becomes[32]

$$\begin{cases} \frac{\partial\rho}{\partial t}+\nabla\cdot(\rho\boldsymbol{U})=0, \\ \frac{\partial(\rho\boldsymbol{U})}{\partial t}+\nabla\cdot(\rho\boldsymbol{U}\otimes\boldsymbol{U})=-\nabla P+\frac{RaPr}{2\varepsilon}\rho\boldsymbol{e}_{g}+Pr\nabla\cdot\boldsymbol{\tau}, \\ \frac{\partial(\rho\Theta)}{\partial t}+\nabla\cdot(\rho\boldsymbol{U}\Theta)=\nabla^{2}\Theta+\left(\frac{\eta-1}{\eta}\right)\frac{\mathrm{d}P_{\mathrm{th}}}{\mathrm{d}t}, \\ P_{\mathrm{th}}=Z\rho\Theta. \end{cases} \tag{14}$$

In Equation (14), Pr is the Prandtl number as defined earlier, η is the heat capacity ratio ($\eta=c_{p}/c_{v}$), and P_{th} is the global dimensionless thermodynamic pressure. In this study, we only present results for an ideal diatomic gas ($Z=1$). Also, $\boldsymbol{\tau}$ is the stress tensor given in dimensionless form by

$$\boldsymbol{\tau}=\nabla\boldsymbol{U}+(\nabla\boldsymbol{U})^{T}-2/3(\nabla\cdot\boldsymbol{U})\boldsymbol{I}. \tag{15}$$

In Equation (15), Stokes' hypothesis ($\lambda=-2/3\mu$) for bulk viscosity is used. In the compressible/weakly-compressible approach, the Rayleigh number is expressed slightly differently compared to the incompressible flow, as

$$Ra=Pr\frac{g{\rho_{0}}^{2}(T_{\mathrm{h}}-T_{\mathrm{c}})L^{3}}{T_{o}{\mu_{0}}^{2}}. \tag{16}$$

Comparing incompressible and compressible Rayleigh number definitions gives an interesting relation for Froude number,

$$\underbrace{2\varepsilon=(T_{\mathrm{h}}-T_{\mathrm{c}})/T_{o}}_{\text{Compressible}}=\underbrace{\beta\Delta\theta=RaPrFr}_{\text{Incompressible}}\rightarrow Fr=2\varepsilon/RaPr. \tag{17}$$

Equation (17) is an important relation that matches the Froude number corresponding to a given relative temperature difference at each Rayleigh and Prandtl number; it additionally demonstrates the required result for isobaric and isochoric thermal expansion in gases, whereby $\alpha=1/T_{0}$. Regarding the maximum possible relative temperature difference value of unity ($\varepsilon_{\max}=1$), the maximum physical Froude number at each Rayleigh and Prandtl number is equal to $2/RaPr$ ($Fr_{\max}=2/RaPr$), which is consistent with Equation (9) for the maximum non-Boussinesq parameter value.

3 | DESCRIPTION OF THE PROBLEM

In this study, the proposed model natural convection problem is the concentric horizontal annulus cavity portrayed in Figure 1. While the symmetry of the geometry naturally lends itself to the use of polar coordinates, the present formulation is developed in a Cartesian framework to permit future generalisation to arbitrary geometries. Boundary conditions are shown in Figure 1A. The inner and outer radii of the annulus are denoted by r_{i} and r_{o}, respectively, with aspect ratio fixed at $r_{o}/r_{i}=2.6$ consistent with published benchmark studies.[8,14,16-19] The region between the two cylinders is filled with air having $Pr=0.71$. The inner and outer cylinders are kept at constant temperatures T_{h} and T_{c}, respectively, with $T_{\mathrm{h}}>T_{\mathrm{c}}$. The reference length, $L_{\mathrm{ref}}=r_{o}-r_{i}$, is equal to the radial gap between the two cylinders. Simulations are carried out for Rayleigh numbers ranging from 10^{1} to 10^{5}, within the steady-state regime for this system.[10-14]

Once the values of the thermo-fluid parameters in the physical domain are obtained, the Nusselt number, entropy generation, and friction coefficient are determined. The local and average Nusselt numbers along the walls of the annulus cavity are obtained from

$$Nu_{\mathrm{loc}}=-\partial\Theta/\partial\widetilde{r}\big|_{\mathrm{wall}} \tag{18}$$

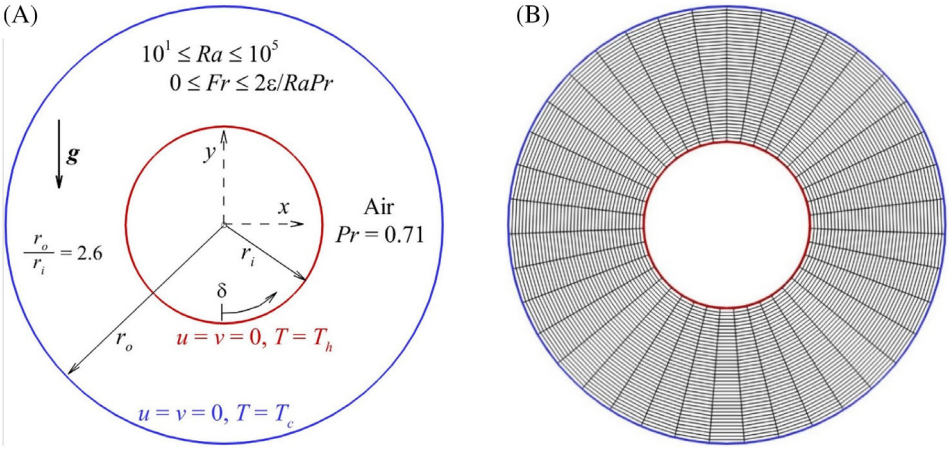

FIGURE 1 The concentric annulus of two circular cylinders. A, Schematic view and boundary conditions; B, A coarse computational grid having 40×40 computational nodes is shown for illustration purposes [Colour figure can be viewed at wileyonlinelibrary.com]

and

$$Nu_{\text{ave}} = \frac{1}{2\pi(r_i + r_o)}\left[\int_0^{2\pi r_o} Nu_{\text{loc},o}\,\mathrm{d}s + \int_0^{2\pi r_i} Nu_{\text{loc},i}\,\mathrm{d}s\right]. \tag{19}$$

The skin friction along the cylinder surfaces is related to the fluid flow via the gradient of the velocity components normal to the surface. In this study, the friction coefficient along the surface based on the dimensionless velocity is defined as

$$c_f = -\frac{\tau_w}{1/2\rho(\alpha/L)^2} = -2Pr\frac{\partial U_\delta}{\partial \boldsymbol{n}}\bigg|_{\text{wall}}. \tag{20}$$

In Equation (18), $\boldsymbol{n}$ is the unit normal vector to the surface. Since the governing equations are solved in a Cartesian coordinate system, the above fundamental definition is implemented through the 2D shear stress tensor as

$$\boldsymbol{c_f} = -2Pr\begin{bmatrix}\tau_{xx} & \tau_{xy}\\ \tau_{yx} & \tau_{yy}\end{bmatrix}\begin{bmatrix}n_x\\ n_y\end{bmatrix} = -2Pr\begin{bmatrix}2\partial U/\partial X & \partial U/\partial Y + \partial V/\partial X\\ \partial U/\partial Y + \partial V/\partial X & 2\partial V/\partial Y\end{bmatrix}\begin{bmatrix}n_x\\ n_y\end{bmatrix}, \tag{21}$$

where n_x and n_y are the horizontal and vertical components of the wall-normal vector, respectively. In this state, the friction coefficient magnitude is calculated as

$$c_f = \sqrt{(c_{f_x})^2 + (c_{f_y})^2} \tag{22}$$

where

$$c_{f_x} = -2Pr[(2\partial U/\partial X)n_x + (\partial U/\partial Y + \partial V/\partial X)n_y], \tag{23}$$

$$c_{f_y} = -2Pr[(\partial U/\partial Y + \partial V/\partial X)n_x + (2\partial V/\partial Y)n_y]. \tag{24}$$

The dimensionless local entropy generation due to heat transfer (S_θ) and fluid friction (S_ψ) are calculated as

$$S_\Theta = \left[\left(\frac{\partial \Theta}{\partial X}\right)^2 + \left(\frac{\partial \Theta}{\partial Y}\right)^2\right], \tag{25}$$

$$S_\psi = \chi\left[2\left\{\left(\frac{\partial U}{\partial X}\right)^2 + \left(\frac{\partial V}{\partial Y}\right)^2\right\} + \left(\frac{\partial U}{\partial Y} + \frac{\partial V}{\partial X}\right)^2\right], \tag{26}$$

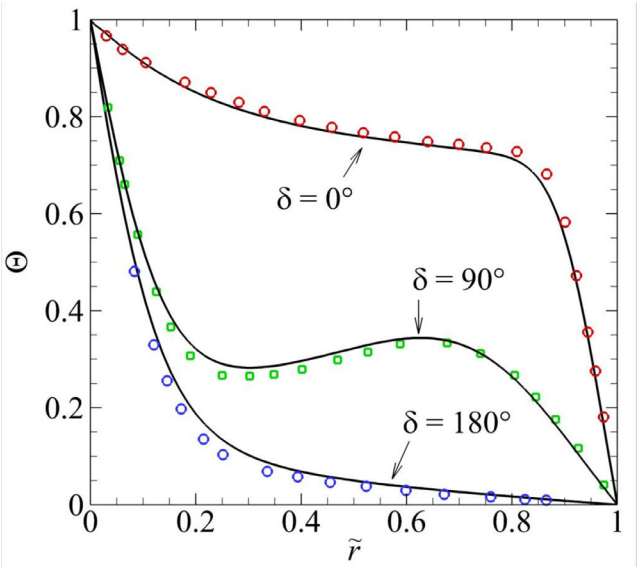

FIGURE 2 Comparison of profiles at $Ra = 5 \times 10^4$ and $Pr = 0.706$ using the present scheme (lines) and Kuhen and Goldstein[8] (symbols) at shown angles [Colour figure can be viewed at wileyonlinelibrary.com]

where in Equation (24), χ is the irreversibility distribution ratio related to the fluid friction irreversibility defined as

$$\chi = \frac{\mu T_0}{k}\left(\frac{\alpha}{L\Delta\theta}\right)^2. \tag{27}$$

The irreversibility distribution ratio assumed to be fixed and equal to 10^{-4} in this study. A similar value for χ was considered in References 33, 34. The total entropy generation due to heat transfer and fluid friction can be calculated by the summation of the local entropy generation over the physical domain via

$$S_{\Theta,\text{tot}} = \int_V S_\Theta \, \mathrm{d}v \tag{28}$$

and

$$S_{\psi,\text{tot}} = \int_V S_\psi \, \mathrm{d}v. \tag{29}$$

The relative dominance of entropy generation due to heat transfer and fluid friction is characterized by the average Bejan number (Be_{ave}), a dimensionless parameter defined as[35-37]

$$Be_{\text{ave}} = \frac{S_{\Theta,\text{tot}}}{S_{\Theta,\text{tot}} + S_{\psi,\text{tot}}}. \tag{30}$$

Values of $Be_{\text{ave}} > 0.5$ imply the dominance of the heat transfer irreversibility and $Be_{\text{ave}} < 0.5$ implies dominance of fluid friction irreversibility.

For the numerical solution of the governing equations, a control volume finite-element method (CVFEM) is used that implements the method of proper closure equation (MPCE)[38] and co-located variables. The problem is two-dimensional and steady. The advection terms are approximated by a second-order upwind scheme and the diffusion terms are discretized using a second order central differentiation scheme. Convergence criteria is considered as the maximum variation of the velocity and temperature fields over all nodes during two successive iterations less than 10^{-7}. Accurate performance of the developed solver has already been validated in References 39-46, but here it is evaluated by comparing the radial temperature profiles at three different angles including $\delta = 0^o$, 90^o, and 180° vs dimensionless radius ($\tilde{r} = r - r_i/r_o - r_i$) at $Ra = 5 \times 10^4$ for air with $Pr = 0.706$. Computed profiles are plotted in Figure 2 and are compared with the results of Kuhen and Goldstein.[8] A close agreement is observed.

TABLE 1 Comparison of the calculated average equivalent heat conductivities along the inner and outer cylinders to the available data

	Reference	$\overline{k}_{eq,i}$ (Error)	$\overline{k}_{eq,o}$ (Error)
$Ra = 10^3$	Kuhen and Goldstein[8]	1.081 (1.08%)	1.084 (1.08%)
	Ashrafizadeh and Nikfar[14]	1.082 (0.99%)	1.082 (1.26%)
	Najafi and Enjilela[16]	1.083 (0.89%)	1.093 (0.26%)
	Wu et al[17]	1.076 (1.54%)	1.087 (0.80%)
	Ho-Minh et al[18]	1.080 (1.17%)	1.079 (1.53%)
	Shu[19]	1.082 (0.99%)	1.082 (1.26%)
	Present Study	**1.092**	**1.095**
$Ra = 10^4$	Kuhen and Goldstein[8]	2.010 (0.65%)	2.005 (0.55%)
	Ashrafizadeh and Nikfar[14]	1.979 (0.89%)	1.980 (1.79%)
	Najafi and Enjilela[16]	2.022 (1.25%)	2.090 (3.66%)
	Wu et al[17]	1.998 (0.05%)	2.084 (3.36%)
	Ho-Minh et al[18]	1.967 (1.49%)	1.953 (3.13%)
	Shu[19]	1.979 (0.89%)	1.979 (1.84%)
	Present Study	**1.996**	**2.016**
$Ra = 5 \times 10^4$	Kuhen and Goldstein[8]	3.024 (0.90%)	2.973 (2.06%)
	Ashrafizadeh and Nikfar[14]	2.958 (1.29%)	2.960 (2.48%)
	Najafi and Enjilela[16]	2.932 (2.16%)	2.992 (1.43%)
	Ho-Minh et al[18]	2.946 (1.69%)	2.866 (5.58%)
	Shu[19]	2.958 (1.29%)	2.958 (2.55%)
	Present Study	**2.99**	**3.03**
$Ra = 7 \times 10^4$	Kuhen and Goldstein[8]	3.308 (2.10%)	3.226 (1.69%)
	Ashrafizadeh and Nikfar[14]	3.193 (1.44%)	3.196 (2.60%)
	Najafi and Enjilela[16]	3.208 (0.97%)	3.102 (5.47%)
	Ho-Minh et al[18]	3.182 (1.78%)	3.070 (6.44%)
	Present Study	**3.23**	**3.28**
$Ra = 10^5$	Ashrafizadeh and Nikfar[14]	3.462 (1.59%)	3.464 (1.47%)
	Najafi and Enjilela[16]	3.497 (0.59%)	3.419 (2.75%)
	Present Study	**3.518**	**3.516**

Accuracy of the solver is also evaluated by computing the equivalent inner cylinder conductivity, $\overline{k}_{eq,i}$, and the average equivalent outer cylinder conductivity, $\overline{k}_{eq,o}$, which are defined for the annulus cavity problem as

$$\overline{k}_{eq,i} = -\frac{\ln(\eta)}{2\pi(\eta-1)} \int_0^{2\pi} \left.\frac{\partial T}{\partial r}\right|_{r=r_i} d\delta, \tag{31}$$

$$\overline{k}_{eq,o} = -\frac{\eta \ln(\eta)}{2\pi(\eta-1)} \int_0^{2\pi} \left.\frac{\partial T}{\partial r}\right|_{r=r_o} d\delta. \tag{32}$$

Results of computed $\overline{k}_{eq,i}$ and $\overline{k}_{eq,o}$ are compared in Table 1 with data reported in References 8, 14, 16-19 at five different Rayleigh numbers. Calculated error percentages shows a pleasing agreement between the computational results and the available data.

A mesh dependency test was conducted, and it was found that a 181×181 computational grid achieves convergence of numerical computations to six significant figures for average Nusselt number. The mesh sensitivity analysis vs mesh

TABLE 2 Mesh sensitivity analysis at $Ra = 10^5$

No. radial nodes × No. axial nodes	$\overline{k}_{eq,i}$	$\overline{k}_{eq,o}$
91 × 91	3.489367	3.509973
121 × 91	3.509823	3.510798
151 × 121	3.517114	3.512402
181 × 151	3.518266	3.514339
181 × 181	3.518479	3.516452
361 × 361	3.518479	3.516452

refinement is presented in terms of inner and outer cylinder equivalent conductivities in Table 2. For illustration purposes, a lower-resolution mesh is shown in Figure 1B.

4 | RESULTS AND DISCUSSION

In this section, the results obtained using each of the classic Boussinesq approximation, proposed approximation and weakly compressible approach are presented. Throughout this study, Fr is altered between a small relative temperature difference representative of the Boussinesq case ($\varepsilon_B = 0.01$) and a large relative temperature difference beyond the validity of the Boussinesq approximation ($\varepsilon_{nB} = 0.2$). Both are computed by Equation (17) at a given Rayleigh and Prandtl number, that is, $2\varepsilon_B/RaPr \le Fr \le 2\varepsilon_{nB}/RaPr$, yielding a range $0.02/RaPr \le Fr \le 0.4/RaPr$ for Froude number. In all simulations reported in this article, the flows were consistently found to be symmetrical about the vertical centreline of the annulus. Also, for the investigated range of the Froude number and Rayleigh number ($10 \le Ra \le 10^5$), it is supposed that the flow field is 2D and stable. It is presently unknown when and how these flows bifurcate from the steady 2D solution branch. It would be interesting for future studies to elucidate the stability of this system.

To appreciate the role of the added term $RaPr\Theta(\,Fr(\boldsymbol{U}\cdot\nabla)\boldsymbol{U})$ in the momentum equation, simulations are conducted at $Ra = 10^5$ under the three models with $\varepsilon = 0.2$, with resulting thermo-flow fields shown in Figure 3. This corresponds to a Gay-Lussac parameter value of $Ga = \beta\Delta\theta = RaPrFr = 0.4$. The flow field corresponding to the proposed model can be seen to be slightly different at this ε from the Boussinesq solution in the upper half of the enclosure where natural convection is stronger. In the solution corresponding to the proposed model, the location of the maximum stream function has shifted slightly transversely away from the vertical centre-line. Comparing the stream-function fields in Figure 3A,B,D under the three approaches, the proposed method more closely resembles the weakly compressible result than the Boussinesq solution does. In addition, this similarity bears out in the temperature fields, particularly near the upper part of the inner cylinder, where the proposed method and weakly compressible approach exhibit a wider plume rising from the top of the inner cylinder.

Further insights into the action of the non-Boussinesq buoyancy effects may be gleaned by considering the acceleration field generated by the extra term in the momentum equation (ie, the right-most term in Equation (10). The magnitude of the non-Boussinesq acceleration field generated from the Boussinesq flow field (ie, $|\Theta((\boldsymbol{U}\cdot\nabla)\boldsymbol{U})|$) from Figure 3A is shown in Figure 3D. It shows that the non-Boussinesq accelerations are strongest at the base of the plume rising from the top of the inner cylinder, with weaker effects extending around the surface of the inner cylinder, within the plume approximately half-way between inner and outer cylinders, and near to the outer cylinder across the lower half of the domain. The magnitude of the field is close to zero in the lower regions of the cavity, which correspond to the regions of greatest similarity between the Boussinesq and non-Boussinesq cases compared in Figure 3A,B.

Finally, to understand the directionality of the action of the non-Boussinesq effect, "streamlines" (strictly, lines everywhere tangent to the acceleration vector field) of the non-Boussinesq acceleration field are plotted in Figure 3A. Notable features in this plot in the context of the distortion of the non-Boussinesq solution from its Boussinesq counterpart include the following: with the exception of the vertical centreline, the tangent lines near the inner cylinder point inward toward its surface, explaining the thinner thermal boundary layer in the non-Boussinesq case (Figure 3B); tangent lines exhibit a strong horizontal extension field approximately one-third of the distance from the top of the inner cylinder to the outer cylinder along the centreline, explaining the wider thermal plume seen in the non-Boussinesq case; above this location either side of the centreline the tangent lines point uniformly down and outward, explaining the greater spread of hotter fluid expelled by the plume near the top of the cavity in the non-Boussinesq case; tangent lines converge to a

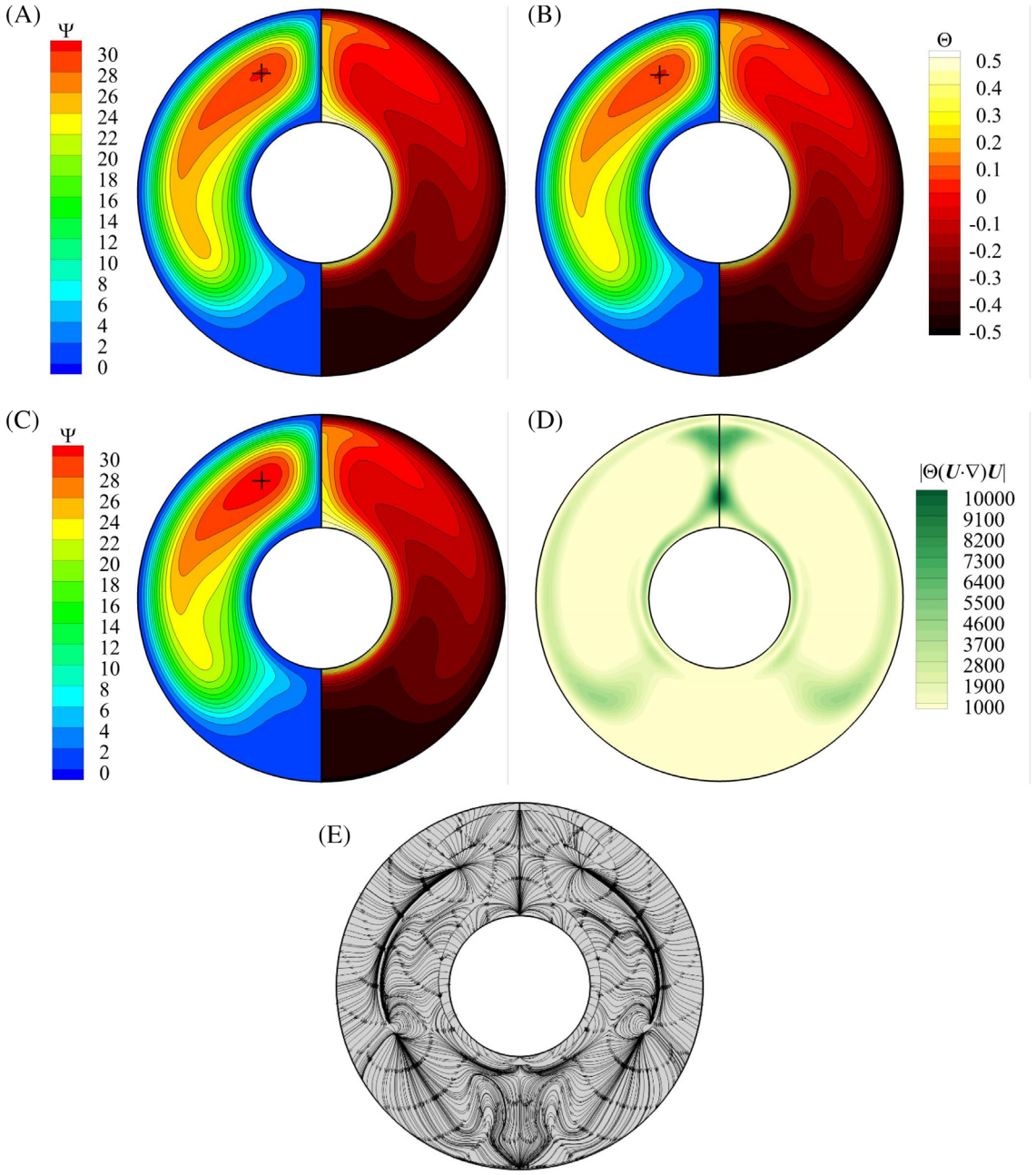

FIGURE 3 Results computed for $Pr = 0.71$, $Ra = 10^5$, and $\varepsilon = 0.2$, A, under the Boussinesq approximation; B, the proposed approximation with $Fr = 0.4/RaPr$, C, weakly compressible approach. Contours depict stream function (left half) and temperature (right half), and "+" identifies the point of maximum stream function. D, Magnitude of the acceleration vector field of the non-Boussinesq acceleration term, where light to dark shading denotes small to large magnitudes. E, "Streamlines" (lines everywhere tangent to the vector field) of the non-Boussinesq acceleration term [Colour figure can be viewed at wileyonlinelibrary.com]

sink at $(X, Y) \cong (\pm 0.53, 1.05)$ which is near to the location that the point of maximum stream-function shifts to in the non-Boussinesq case.

4.1 | Local Nusselt number

The local Nusselt number distribution along the inner cylinder is plotted in Figure 4. It should be noted that, to compensate for the different dimensionless temperature definitions between the weakly compressible and incompressible

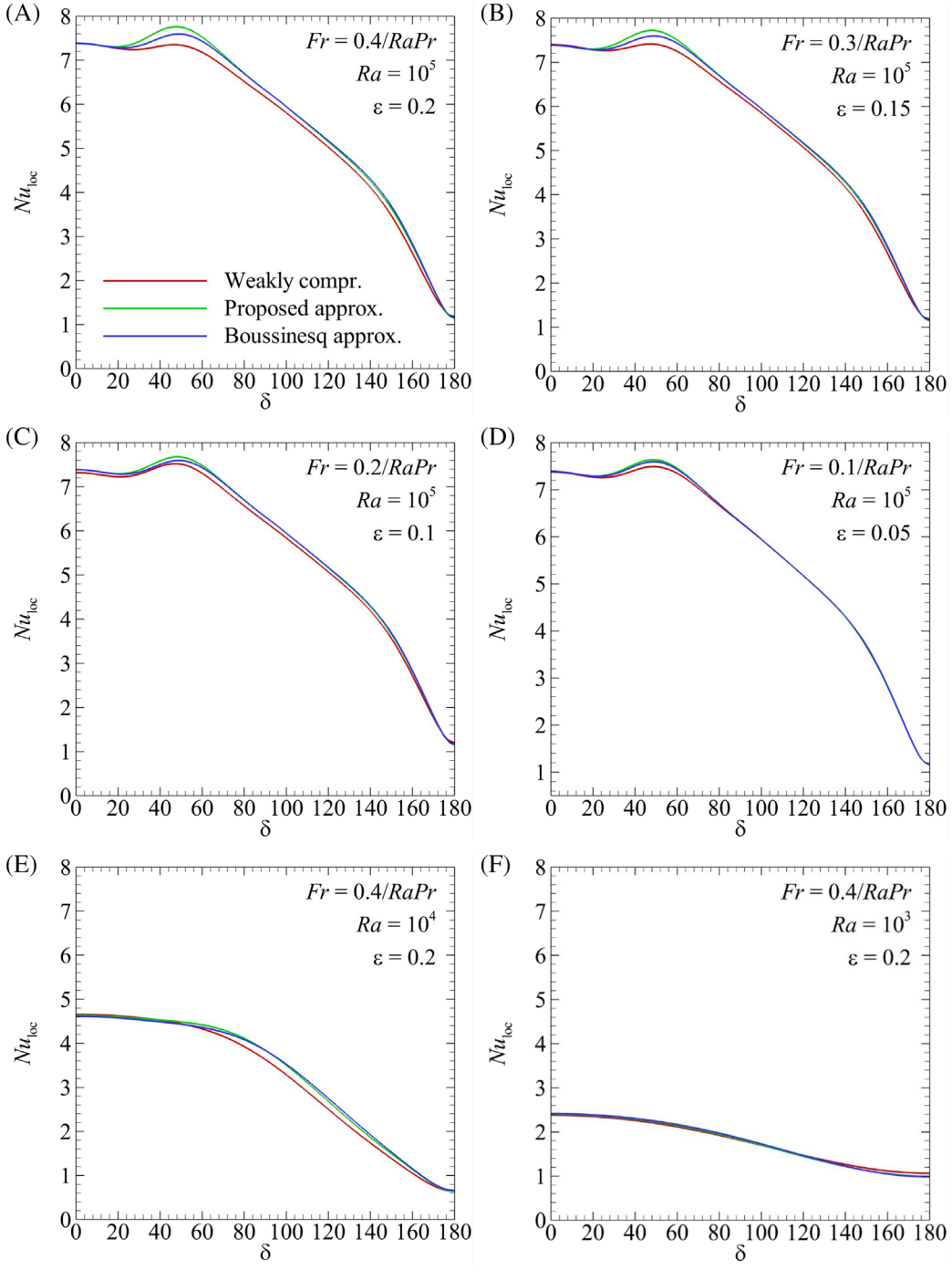

FIGURE 4 Local Nusselt number distribution along the inner cylinder for *Fr* values as stated, at $Pr = 0.71$ and, A-D, $Ra = 10^5$, E, $Ra = 10^4$, and F, $Ra = 10^3$ [Colour figure can be viewed at wileyonlinelibrary.com]

approaches, compressible Nusselt numbers are multiplied by $1/2\varepsilon$. Because of symmetry, only half of the local Nusselt number distribution is shown ($0^o \leq \delta \leq 180^o$). It was found that the mismatch of local Nusselt number distribution along both surfaces is negligible for Froude number lower than $0.1/RaPr$ ($\varepsilon = 0.05$) across the investigated range of the Rayleigh number for different approaches used in this study. Thus, for clarity, only the results of Froude number corresponding to $\varepsilon = 0.05$, 0.1, 0.15, and 0.2 are shown. For the inner cylinder, the local Nusselt number decreases from $\delta = 0^o$ to 180^o with a local peak at approximately $\delta = 50^o$. At $Ra = 10^5$, there is a considerable mismatch between computed local Nusselt number between the different approaches at Froude numbers corresponding to $\varepsilon = 0.15$ and 0.2 compared to lower Froude numbers throughout the range of angular positions. For these two Froude numbers, the local Nusselt number

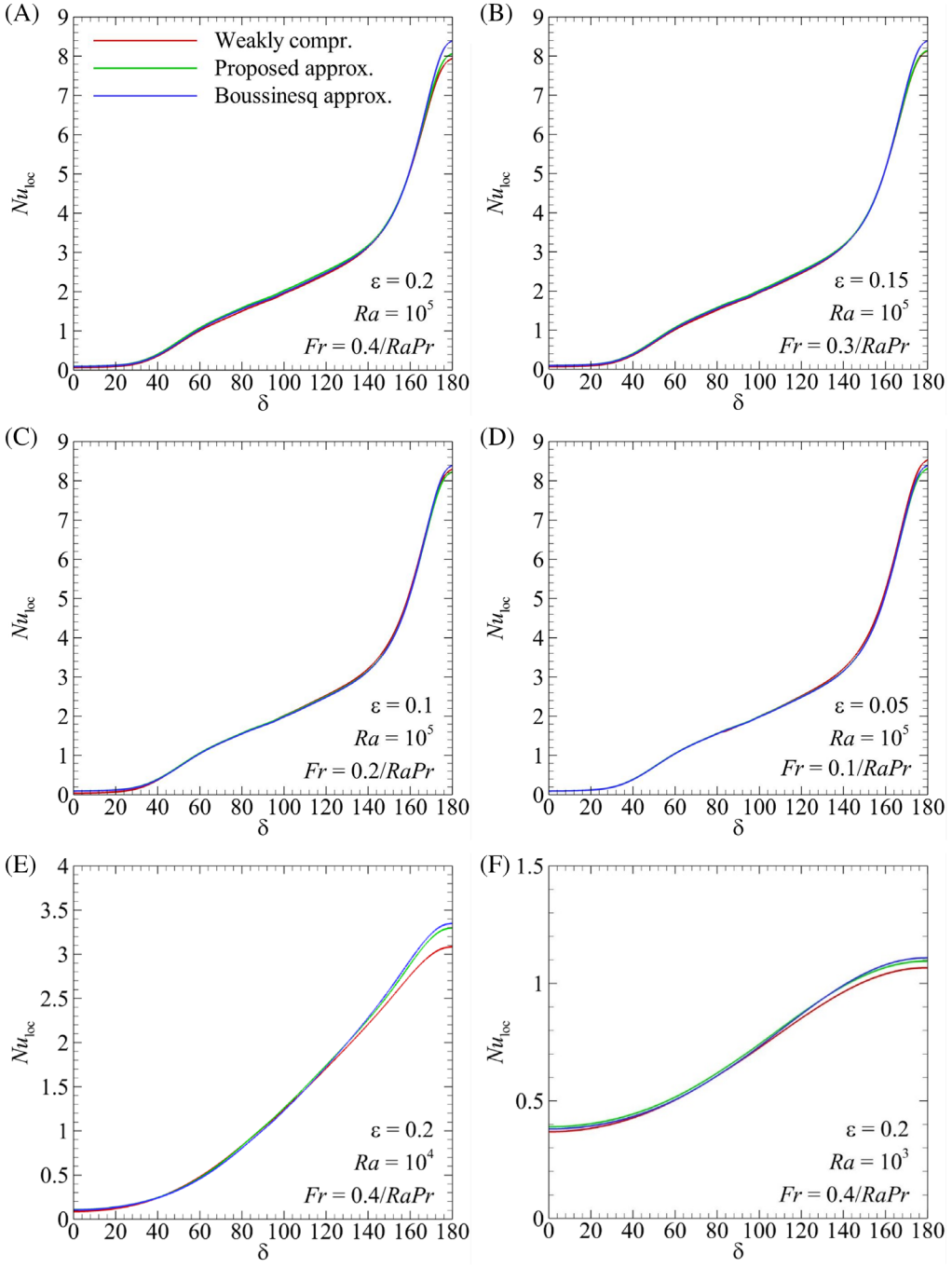

FIGURE 5 Local Nusselt number distribution along the outer cylinder for *Fr* values as shown, at $Pr = 0.71$ and, A-D, $Ra = 10^5$, E, $Ra = 10^4$, and, F, $Ra = 10^3$ [Colour figure can be viewed at wileyonlinelibrary.com]

distribution along the inner surface obtained with the weakly compressible approach shows a lower value compared to the Boussinesq and new approximations. As shown, calculated local Nusselt number distribution under the Boussinesq approximation shows less deviation from the weakly compressible approach compared to the proposed approximation. This may be attributed to the linear density state relation, which is designed for a Boussinesq case with small Gay-Lussac number ($Ga \leq 0.01$). We notice that for $\epsilon = 0.05$ both the Boussinesq and proposed approximations exhibit almost identical results to the weakly compressible approach in Figure 4D. Results from lower Rayleigh numbers, $Ra = 10^4$ and 10^3 (Figure 4E,F), show almost the same results for the three approaches used in this study even for large relative temperature difference applied in this study ($\epsilon = 0.2$), concluding that the effect of a large Gay-Lussac number is much important in convection dominated regimes in natural convection problems.

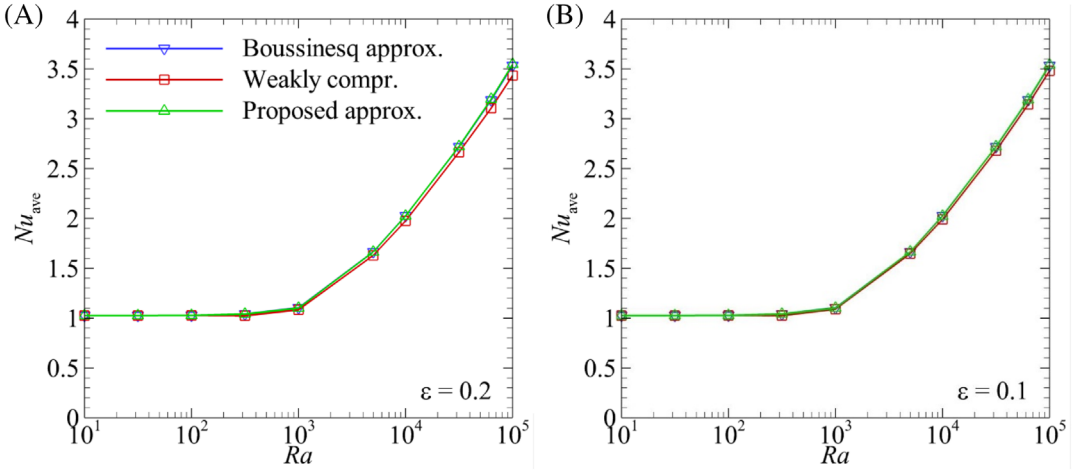

FIGURE 6 A plot of average Nusselt number against Rayleigh number for different ϵ values as shown [Colour figure can be viewed at wileyonlinelibrary.com]

Distribution of the local Nusselt number along the outer cylinder is shown in Figure 5. For the outer cylinder, the local Nusselt number increases from $\delta = 0^o$ to $\delta = 180^o$. Along this surface, distribution of the local Nusselt number for different ϵ are almost identical at $Ra = 10^5$ (Figure 5A-D). Regarding stronger natural convection along the inner hot wall where the plume forms, this negligible difference between different approaches may be attributed to the weaker natural convection effect along the outer cold cylinder. Decreasing by one order to $Ra = 10^4$ (Figure 5E), a deviation between weakly compressible and Boussinesq type approximations is formed that is annihilated by decreasing one extra order to $Ra = 10^3$ (Figure 5F). Results over $Fr \leq 0.1/RaPr$ (non-Boussinesq approximation) and $Fr = 0$ (Boussinesq approximation) yield almost the same results to the weakly compressible approach in the range of investigated Rayleigh numbers. Hence the results from small relative temperature differences are not presented here.

4.2 | Average Nusselt number

The variation in the average Nusselt number with Rayleigh number ($10 \leq Ra \leq 10^5$) for relative temperature differences $\epsilon = 0.2$ and 0.1 ($Fr = 0.4/RaPr$ and $Fr = 0.2/RaPr$, respectively) is plotted in Figure 6. In order to evaluate Equation (19), Simpson's 1/3rd rule of integration is used. As predicted, the average Nusselt number is increased by increasing the Rayleigh number. Across the computed range of Rayleigh number, obtained results for $Fr \leq 0.2/RaPr$ ($\epsilon = 0.1$) are giving similar results with a negligible difference between different approaches, which is why average Nusselt number results for $\epsilon < 0.1$ are not presented here. Figure 6 indicates that by increasing the Rayleigh number, the Boussinesq and proposed approximations start to deviate from the weekly compressible approach at around $Ra = 10^4$, where the heat transfer mechanism becomes convection dominated. Also, the difference between Boussinesq and proposed approximation across the investigated range of Rayleigh number is negligible at least up to $\epsilon = 0.2$. Both approximations show deviation from the weakly compressible approach in the convection dominated regime. Comparison of the average Nusselt number at $Ra = 10^5$ for $\epsilon = 0.2$ reveals a respective 3.25% and 2.89% mismatch between proposed and Boussinesq approximations compared to the weakly compressible approach. The slight deviation of obtained results via proposed approximation from weakly compressible in average Nusselt number at high Rayleigh number may be attributed to the linear definition of the density state relation, which is designed for small relative temperature difference.

4.3 | Skin shear stress

The next quantity to be considered is coefficient of friction over the surface of the cylinders. Results are shown for $10^3 \leq Ra \leq 10^5$ and $0.05 \leq \epsilon \leq 0.2$ in Figures 7 and 8 for the inner and outer cylinders, respectively. Since for $\epsilon \leq 0.05$ results of different approaches are hardly distinguishable, they are not presented here. For $Ra \leq 10^3$ where the heat transfer

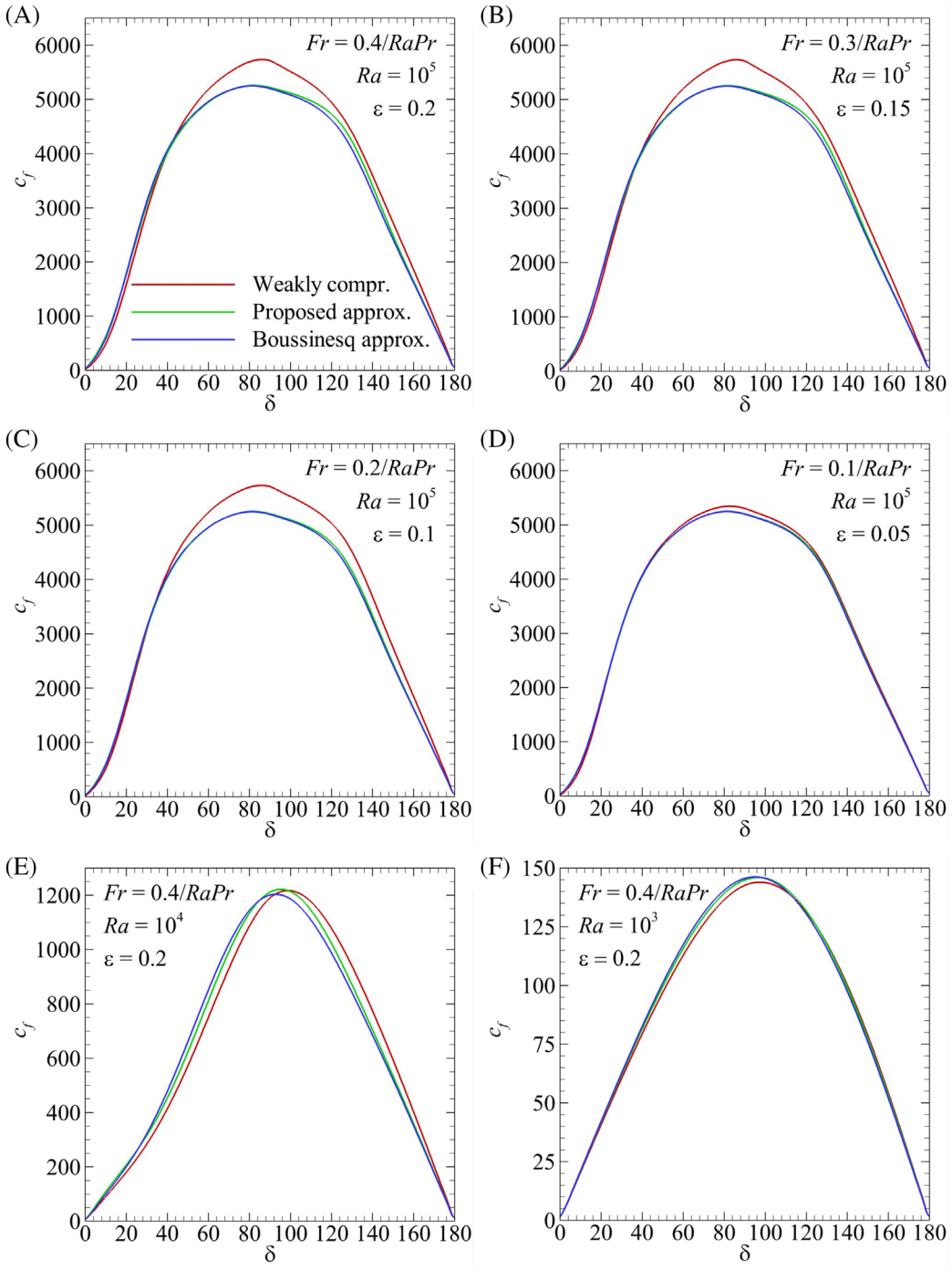

FIGURE 7 Skin friction coefficient distribution along the inner cylinder at stated *Fr* values and Rayleigh numbers, A-D, $Ra = 10^5$, E, $Ra = 10^4$, and, F, $Ra = 10^3$ [Colour figure can be viewed at wileyonlinelibrary.com]

is conduction dominated, results of the different approaches are almost identical even for large relative temperature differences. At $Ra \geq 10^4$, results of the Boussinesq and proposed approximation are not in agreement with the weakly compressible approach having $\varepsilon \geq 0.05$. A comparison of the coefficient of friction along the inner cylinder (Figure 7) reveals that the proposed approximation is giving slightly closer results to the weakly compressible approach compared to the Boussinesq approximation within the convection dominated regime (Figure 7A-D). Better performance of the proposed approximation in approximating flow field gradients becomes more evident for conduction dominated regime and large relative temperature difference (Figure 7E,F). Along the outer cylinder (Figure 8) aside from around $\delta \cong 10^o$ for convection dominated regime (Figure 8A-D), the proposed approximation is superior to the Boussinesq approximation in

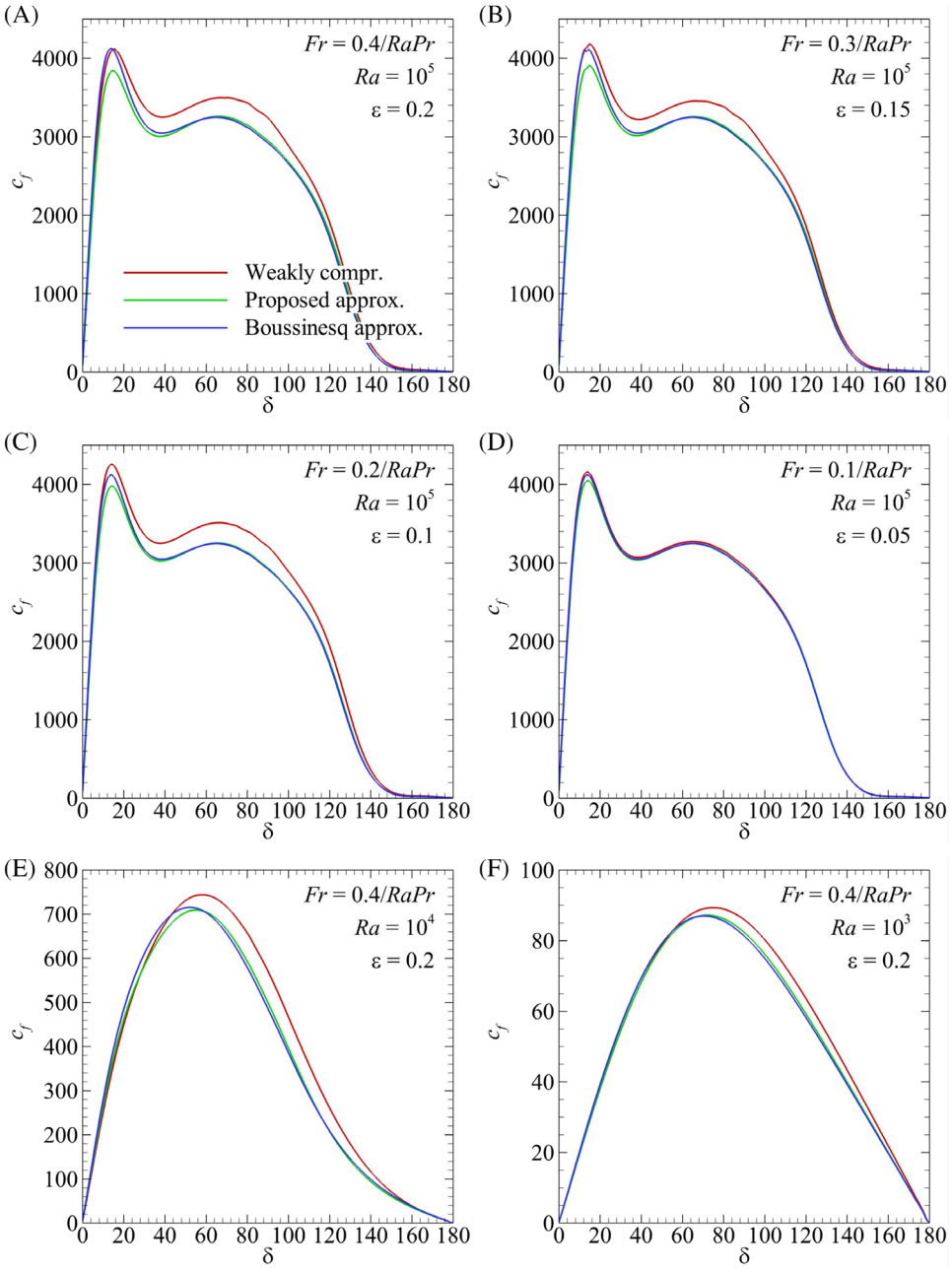

FIGURE 8 Skin friction coefficient distribution along the inner cylinder at stated *Fr* values and Rayleigh numbers, A-D, $Ra = 10^5$, E, $Ra = 10^4$, and, F, $Ra = 10^3$ [Colour figure can be viewed at wileyonlinelibrary.com]

estimating the flow field gradients. As with the inner cylinder, this is more clear as the convection effects diminish toward a conduction dominated regime especially at large ε values (Figure 7E,F). Flow-wise, better performance of the proposed approximation may be attributed to the extension of density variation to advection over the Boussinesq approximation.

4.4 | Entropy generation analysis

The dependence of the average Bejan number on the Rayleigh number will now be investigated over $10 \leq Ra \leq 10^5$ for $\varepsilon = 0.1$ and 0.2. As shown in Figure 9, by increasing the Rayleigh number, the average Bejan number is decreased. This is because by increasing the Rayleigh number, thermal convection increasingly becomes the dominant mechanism driving the flow, in turn producing thinner plum and thermal boundary layer structures, which in turn are subjected to irreversible heat transport via conduction along the steep thermal gradients. This is illustrated in the thermal fields in Figure 3. Notice the thinner thermal boundary layer on the inner cylinder and the stronger plume at $\varepsilon = 0.05$ vs $\varepsilon = 0.2$, which reflects the higher average Nusselt number (Figure 6) and lower Bejan number (Figure 9) seen at $Ra = 10^5$. Note

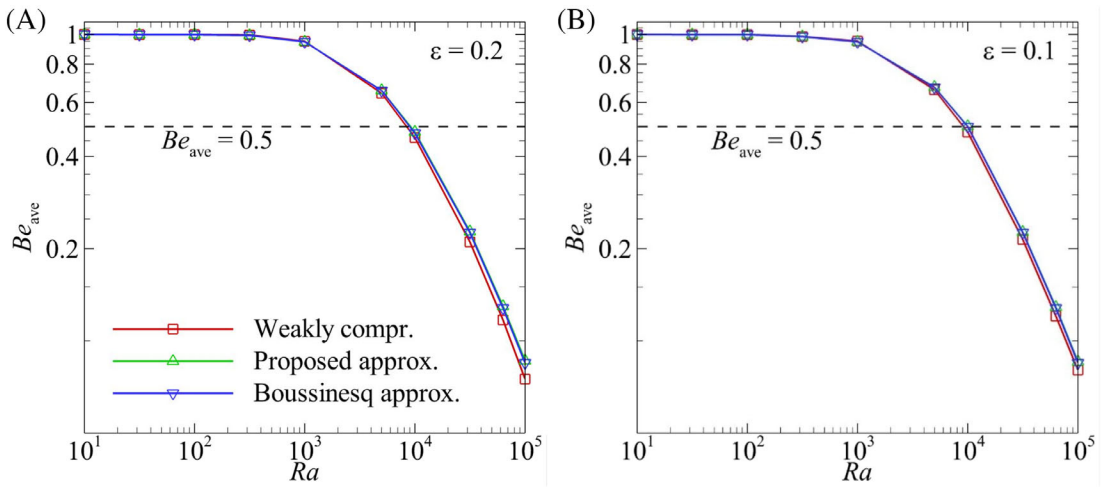

FIGURE 9 A plot of average Bejan number against Rayleigh number for two ε values as shown [Colour figure can be viewed at wileyonlinelibrary.com]

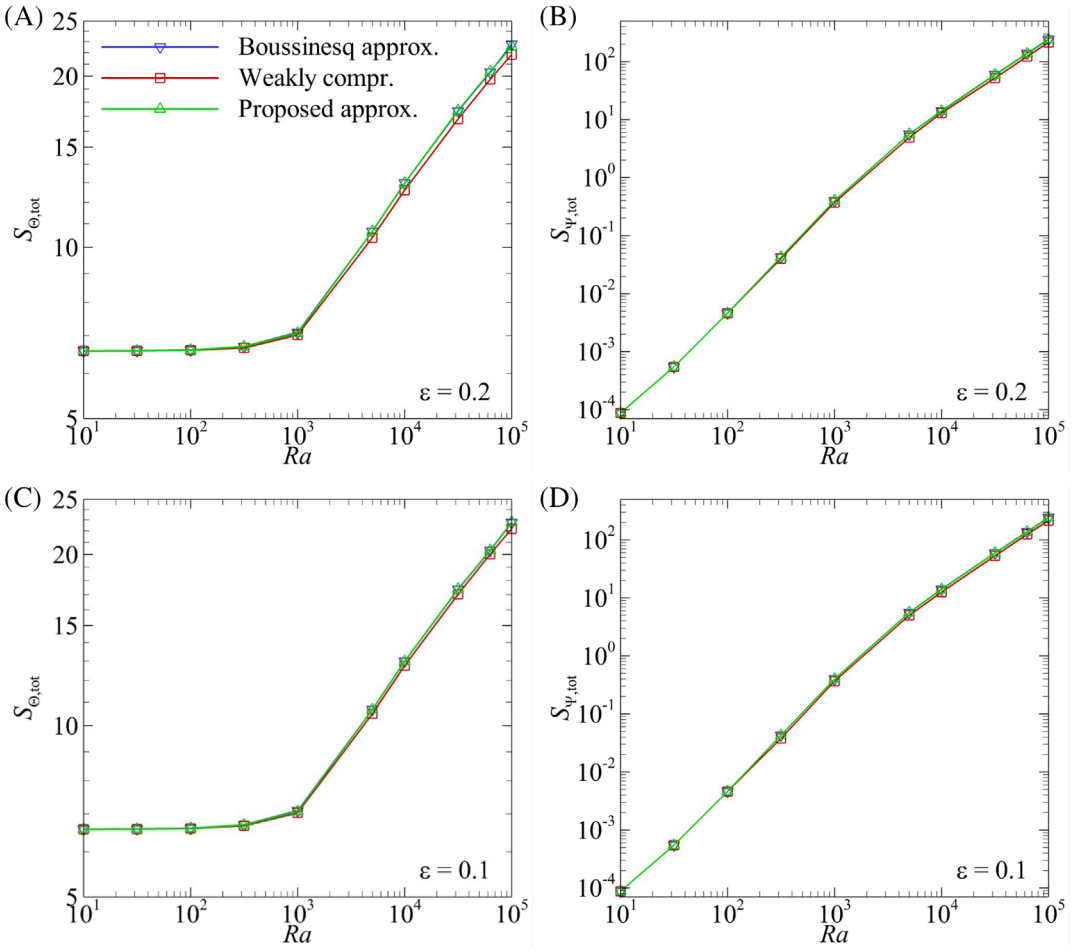

FIGURE 10 A plot of total entropy generation due to, A,C, heat transfer:$S_{\Theta,\,tot}$, B,D, fluid friction: $S_{\psi,\,tot}$ for two ε values as shown [Colour figure can be viewed at wileyonlinelibrary.com]

that, for $Ra > 10^4$, the average Bejan number is smaller than 0.5, which means that most of the irreversibility is due to convection heat transfer. For $Ra < 10^4$, where conduction is still the dominant mechanism, the average Bejan number has a value larger than 0.5, indicating that the majority of generated irreversibility is due to fluid friction.

Similar to the average Nusselt number, both the Boussinesq and proposed approximations show similar results up to $\varepsilon = 0.2$ with a negligible difference of order 10^{-3}. A noticeable mismatch between the Boussinesq type approaches and the weakly compressible approach is observed at $Ra = 10^5$. Obtained results demonstrate that the Boussinesq type approximations exhibit 6.47% and 14.93% higher values for $\varepsilon = 0.1$ and 0.2, respectively. This means that the non-Boussinesq effects have created a tendency for the flow to bias slightly toward fluid friction irreversibility rather than heat transfer irreversibility.

The rate of total entropy generation due to heat transfer ($S_{\Theta,\,\mathrm{tot}}$) and fluid friction ($S_{\psi,\,\mathrm{tot}}$) is also investigated separately over $10 \leq Ra \leq 10^5$ for $\varepsilon = 0.1$ and 0.2 in Figure 10. Irrespective of ε value, by increasing the Ryleigh number, the magnitude of both entropies is increased, but this is more evident for entropy generation due to fluid friction ($S_{\psi,\,\mathrm{tot}}$). As mentioned before, by increasing Rayleigh number, convection becomes the dominant part of the heat transfer mechanism and the share of conduction in heat transfer is decreased. This describes the continuing growth rate of entropy generation due to fluid friction in Figure 10B,D vs slow growth rate of entropy generation due to heat transfer in Figure 10A,C. In the range of investigated entropy generation up to $\varepsilon = 0.2$, the difference between Boussinesq type approximations is small, of order 10^{-3}. At $Ra = 10^5$ and $\varepsilon = 0.2$, a noticeable mismatch of 4.28% and 11.57% is observed for $S_{\Theta,\,\mathrm{tot}}$ and $S_{\psi,\,\mathrm{tot}}$, respectively.

5 | CONCLUSIONS

In this study, a new approximation is proposed for natural convention problems in Cartesian coordinates. In this formulation, Froude number is introduced, characterising deviation from the classic Boussinesq approximation. In addition, a relation is established that matches the Froude number to the relative temperature difference at a given Rayleigh and Prandtl number. The proposed formulation is applied to natural convection in a concentric horizontal annulus cavity with aspect ratio of 2.6 ($r_o/r_i = 2.6$) and results are compared in terms of the local and average Nusselt number, average Bejan number, and skin friction. Obtained results under the proposed approximation show a close agreement with the results under the Boussinesq and weakly compressible approach up to $\varepsilon = 0.05$ for this problem but as the relative temperature difference exceeds 0.05, the results from the different approximations start to deviate from each other, especially in the convection-dominated regime. Obtained results indicate that the proposed Boussinesq type model is superior in its capture of momentum, but is not necessarily better than the traditional Boussinesq approximation in its description of energy. In the context of the Gay-Lussac parameter, the present results demonstrate that the traditional Boussinesq approximation is accurate up to at least $\beta\Delta\theta = RaPrFr = O(10^{-2})$, with deviations being significant approaching values of order unity. It would, therefore, be expected that non-Boussinesq effects would be significant at higher Rayleigh numbers, small-scale systems, or for fluids having large thermal expansion coefficients. For example, ammonia and R-12 refrigerant dichlorodifluoromethane have $\beta \approx 2.5 \times 10^{-3}$ K^{-1} compared to water (2.14×10^{-4} K^{-1}), yielding Fr more than two orders of magnitude greater at the same scale. Finally, the proposed formula is applied here for the laminar regime and horizontal annulus cavity but its extension to turbulent regime and complex geometries is of interest for future studies.

ACKNOWLEDGEMENTS

This research was supported by the Australian Research Council through Discovery Projects DP150102920 and DP180102647. P. M. is supported by a Monash Graduate Scholarship and a Monash International Postgraduate Research Scholarship. The authors are also supported by time allocations on the National Computational Infrastructure (NCI) peak facility and the Pawsey Supercomputing Centre through NCMAS grants. NCI is supported by the Australian Government.

NOMENCLATURE

Be_{ave}	average Bejan number
c_f	skin friction coefficient
e_g	unit vector in gravity direction
Fr	Froude number
g	gravitational acceleration
Ga	Gay-Lussac number ($\beta\Delta\theta$)
L_{ref}	reference length

Nu_{ave}	average Nusselt number
Nu_{loc}	local Nusselt number
P	pressure
p^*	modified pressure
P	dimensionless pressure
P_{th}	thermodynamic pressure
Pr	Prandtl number
R	ideal gas constant
R	radius
r_i	inner cylinder radius
r_o	inner cylinder radius
$\widetilde{r}$	dimensionless radius
Ra	Rayleigh number
S	entropy generation
S_Θ	entropy generation due to heat transfer
S_ψ	entropy generation due to fluid friction
T	temperature
x	horizontal coordinate
X	dimensionless horizontal coordinate
y	vertical coordinate
Y	dimensionless vertical coordinate
$\boldsymbol{U}$	velocity vector
$\boldsymbol{U}$	dimensionless velocity vector
U_δ	angular dimensionless velocity vector
α	thermal diffusivity
β	volumetric thermal expansion coefficient
δ	angle along the cylinders
ϵ	relative temperature difference
θ	physical temperature
Θ	dimensionless temperature
κ	thermal conductivity
μ	kinematic dynamic viscosity
ν	kinematic viscosity
ρ	density
ρ_0	reference density
τ_w	wall shear stress
ϕ	gravitational potential
χ	irreversibility distribution ratio

SUBSCRIPT

ave	average
c	cool
h	hot
loc	local
ref	reference
tot	total

ORCID

Peyman Mayeli https://orcid.org/0000-0003-4084-2627

REFERENCES

1. Varol Y, Oztop HF. A comparative numerical study on natural convection in inclined wavy and flat-plate solar collectors. *Build Environ*. 2008;43(9):1535-1544. https://doi.org/10.1016/j.buildenv.2007.09.002.

2. Tonui JK, Tripanagnostopoulos Y. Improved PV/T solar collectors with heat extraction by forced or natural air circulation. *Renew Energy*. 2007;32(4):623-637. https://doi.org/10.1016/j.renene.2006.03.006.
3. Tonui JK, Tripanagnostopoulos Y. Performance improvement of PV/T solar collectors with natural air flow operation. *Sol Energy*. 2008;82(1):1-12. https://doi.org/10.1016/j.solener.2007.06.004.
4. Wells AJ, Worster MG. A geophysical-scale model of vertical natural convection boundary layers. *J Fluid Mech*. 2008;609:111-137. https://doi.org/10.1017/S0022112008002346.
5. Wettlaufer JS, Worster MG, Huppert HE. Natural convection during solidification of an alloy from above with application to the evolution of sea ice. *J Fluid Mech*. 1997;344:291-316. https://doi.org/10.1017/S0022112097006022.
6. Boussinesq J. *Theorie Analytique de la Chaleur, vol. II*. Gauthier-Villars; 1903.
7. Thomas RW, Davis GV. Natural convection in annular and rectangular cavities a numerical study. Paper presented at International Heat Transfer Conference 4, Paris-Versailies, France; 1970.
8. Kuhen TH, Goldstein RJ. An experimental and theoretical study of natural convection in the annulus between horizontal concentric cylinders. *J Fluid Mech*. 1976;74(4):695-719. https://doi.org/10.1017/S0022112076002012.
9. Sheremet MA, Pop I. Natural convection in a horizontal cylindrical annulus filled with a porous medium saturated by a nanofluid using Tiwari and Das' nanofluid model. *Eur Phys J Plus*. 2015;130:107 https://link.springer.com/article/10.1140/epjp/i2015-15107-4.
10. Sheremet MA, Pop I. Free convection in a porous horizontal cylindrical annulus with a nanofluid using Buongiorno's model. *Comput Fluids*. 2015;118:182-190. https://doi.org/10.1016/j.compfluid.2015.06.022.
11. Moukalled F, Acharya S. Natural convection in the annulus between concentric horizontal circular and square cylinders. *J Thermophys Heat Transf*. 1996;10(3):524-531. https://doi.org/10.2514/3.820.
12. Abu-Nada E, Masoud Z, Hijazi A. Natural convection heat transfer enhancement in horizontal concentric annuli using nanofluids. *Int Commun Heat Mass Transf*. 2008;35:657-665. https://doi.org/10.1016/j.icheatmasstransfer.2007.11.004.
13. Ashrafizadeh A, Nikfar M. On the numerical solution of generalized convection heat transfer problems via the method of proper closure equations–part I: description of the method. *Numer Heat Transf B*. 2016;70(2):187-203. https://doi.org/10.1080/10407782.2016.1173456.
14. Ashrafizadeh A, Nikfar M. On the numerical solution of generalized convection heat transfer problems via the method of proper closure equations–part II: application to test problems. *Numer Heat Transf B*. 2016;70(2):204-222. https://doi.org/10.1080/10407782.2016.1173467.
15. Ashorynejad HR, Mohamad AA, Sheikholeslami M. Magnetic field effects on natural convection flow of a nanofluid in a horizontal cylindrical annulus using lattice Boltzmann method. *Int J Therm Sci*. 2013;64:240-250. https://doi.org/10.1016/j.ijthermalsci.2012.08.006.
16. Najafi M, Enjilela V. Natural convection heat transfer at high Rayleigh numbers – extended meshless local Petrov–Galerkin (MLPG) primitive variable method. *Eng Anal Bound Elem*. 2014;44:170-184. https://doi.org/10.1016/j.enganabound.2014.01.022.
17. Wu YL, Liu GR, Gu YT. Application of meshless local Petrov-Galerkin (MLPG) approach to simulation of incompressible flow. *Numer Heat Transf B*. 2005;48(5):459-475. https://doi.org/10.1080/10407790500324763.
18. Ho-Minh D, Mai-Duy N, Tran-Cong T. A galerkin-RBF approach for the streamfunction-vorticity-temperature formulation of natural convection in 2D enclosured domains. *Comput Model Eng Sci*. 2009;44(3):219-248. https://doi.org/10.3970/cmes.2009.044.219.
19. Shu C. Application of differential quadrature method to simulate natural convection in a concentric annulus. *Int J Numer Methods Fluids*. 1999;30:977-993. https://doi.org/10.1002/(SICI)1097-0363(19990830)30:8%3C977::AID-FLD873%3E3.0.CO;2-J.
20. Pepper DW, Harris SD. Numerical simulation of natural convection in closed containers by a fully implicit method. *J Fluids Eng*. 1977;99(4):649-656. http://fluidsengineering.asmedigitalcollection.asme.org/article.aspx?articleid=1424151.
21. Vierendeels J, Merci B, Dick E. A multigrid method for natural convective heat transfer with large temperature differences. *J Comput Appl Math*. 2004;168(1–2):509-517. https://doi.org/10.1016/j.cam.2003.08.081.
22. Becker R, Braack M. Solution of a stationary benchmark problem for natural convection with large temperature difference. *Int J Therm Sci*. 2002;41(5):428-439. https://doi.org/10.1016/S1290-0729(02)01335-2.
23. Szewc K, Pozorski J, Tanière A. Modelling of natural convection with smoothed particle hydrodynamics: non-Boussinesq formulation. *Int J Heat Mass Transf*. 2011;54:4807-4816. https://doi.org/10.1016/j.ijheatmasstransfer.2011.06.034.
24. Lopez JM, Marques F, Avila M. The Boussinesq approximation in rapidly rotating flows. *J Fluid Mech*. 2013;737:56-77. https://doi.org/10.1017/jfm.2013.558.
25. Valori V, Elsinga G, Rhode M, Tummers M, Westerweel J, van der Hagen T. Experimental velocity study of non-Boussinesq Rayleigh-Bénard convection. *Phys Rev 95*. 2017;053113:1-12. https://journals.aps.org/pre/abstract/10.1103/PhysRevE.95.053113.
26. Manga M, Weeraratne D. Experimental study of non-Boussinesq Rayleigh–Bénard convection at high Rayleigh and Prandtl numbers. *Phys Fluids*. 1999;11:2969-2976. https://aip.scitation.org/doi/abs/10.1063/1.870156.
27. Zhang J, Childress S, Libchaber A. Non-Boussinesq effect: thermal convection with broken symmetry. *Phys Fluids*. 1997;9:1034-1042. https://doi.org/10.1063/1.869198.
28. Zhang Y, Cao Y. A numerical study on the non-Boussinesq effect in the natural convection in horizontal annulus. *Phys Fluids*. 2018;30:040902. https://doi.org/10.1063/1.5010864.
29. Paolucci S. On the filtering of sound from the Navier-Stokes equations, Technical report, Sandia National Laboratories. *SAND*. 1982;9:82-8257.
30. Paillere H, Viozat C, Kumbaro A, Toumi I. Comparison of low Mach number models for natural convection problems. *Heat Mass Transf*. 2000;36:567-573. https://doi.org/10.1007/s002310000116.
31. Le Quéré P, Weisman C, Paillère H, et al. Modelling of natural convection flows with large temperature differences: a benchmark problem for low Mach number solvers. Part 1. Reference solutions. *ESAIM: Math Model Numer Anal*. 2005;39(3):609-616. https://doi.org/10.1051/m2an:2005027.

32. Chenoweth DR, Paolucci S. Natural convection in an enclosed vertical air layer with large horizontal temperature differences. *JFM*. 1986;169:173-210. https://doi.org/10.1017/S0022112086000587.
33. Basak T, Kaluri RS, Balakrishnan AR. Effects of thermal boundary conditions on entropy generation during natural convection. *Numer Heat Transf A*. 2011;59(5):372-402. https://doi.org/10.1080/10407782.2011.549075.
34. Ilis GG, Mobedi M, Sunden B. Effect of aspect ratio on entropy generation in a rectangular cavity with differentially heated vertical walls. *Int Commun Heat Mass Transf*. 2008;35(6):696-703. https://doi.org/10.1016/j.icheatmasstransfer.2008.02.002.
35. Bondareva NS, Sheremet MA, Oztop HF, Abu-Hamdeh N. Entropy generation due to natural convection of a nanofluid in a partially open triangular cavity. *Adv Powder Technol*. 2017;28:244-255. https://doi-org.ezproxy.lib.monash.edu.au/10.1016/j.apt.2016.09.030.
36. Sheremet MA, Pop I, Oztop HF, Abu-Hamdeh N. Natural convection of nanofluid inside a wavy cavity with a non-uniform heating: entropy generation analysis. *Int J Numer Methods Heat Fluid Flow*. 2017;27:958-980. https://doi.org/10.1108/HFF-02-2016-0063.
37. Astanina MS, Sheremet MA, Oztop HF, Abu-Hamdeh N. MHD natural convection and entropy generation of ferrofluid in an open trapezoidal cavity partially filled with a porous medium. *Int J Mech Sci*. 2018;136:493-502. https://doi.org/10.1016/j.ijmecsci.2018.01.001.
38. Ashrafizadeh A, Alinia B, Mayeli P. A new co-located pressure-based discretization method for the numerical solution of incompressible Navier-Stokes equations. *Numer Heat Transf B: Fundament*. 2014;67(6):563-589. https://doi.org/10.1080/10407790.2014.992094.
39. Mayeli P, Nili-Ahmadabadi M, Pirzadeh MR, Rahmani P. Determination of desired geometry by a novel extension of ball spine algorithm inverse method to conjugate heat transfer problems. *Comput Fluids*. 2017;154:390-406. https://doi.org/10.1016/j.compfluid.2016.05.022.
40. Hesami H, Mayeli P. Development of the ball-spine algorithm for the shape optimization of ducts containing nanofluid. *Numer Heat Transf A*. 2016;70(12):1371-1389. https://doi.org/10.1080/10407782.2016.1243976.
41. Nikfar M, Mayeli P. Surface shape design in different convection heat transfer problems via a novel coupled algorithm. *ASME: J Heat Transf*. 2018;140(2):1-15. http://heattransfer.asmedigitalcollection.asme.org/article.aspx?articleid=2648964.
42. Mayeli P, Hesami H, Moghaddam MHDF. Numerical investigation of the MHD forced convection and entropy generation in a straight duct with sinusoidal walls containing water-Al_2O_3 nanofluid. *Numer Heat Transf A*. 2017;71(12):1371-1389. https://doi.org/10.1080/10407782.2016.1243976.
43. Mayeli P, Hesami H, Besharati-Foumani H, Niajalili M. Al_2O_3-water nanofluid heat transfer and entropy generation in a ribbed channel with wavy in the presence of magnetic field. *Numer Heat Transf A*. 2018;73(9):604-623. https://doi.org/10.1080/10407782.2018.1461494.
44. Nikfar M, Ashrafizadeh A, Mayeli P. Inverse shape design via a new physical-based iterative solution strategy. *Inverse Probl Sci Eng*. 2015;23(7):1138-1162. https://doi.org/10.1080/17415977.2014.973873.
45. Mayeli P, Nili-Ahmadabadi M, Besharati-Foumani H. Inverse shape design for heat conduction problems via the ball spine algorithm. *Numer Heat Transf B: Fundament*. 2016;69(3):249-269. https://doi.org/10.1080/10407790.2015.1096690.
46. Mayeli P, Nikfar M. Temperature identification of a heat source in conjugate heat transfer problems via an inverse analysis. *Int J Numer Methods Heat Fluid Flow*. 2019;29(10):3994-4010. https://doi.org/10.1108/HFF-05-2018-0193.

How to cite this article: Mayeli P, Sheard GJ. A centrifugal buoyancy formulation for Boussinesq-type natural convection flows applied to the annulus cavity problem. *Int J Numer Meth Fluids*. 2021;93:683–702. https://doi.org/10.1002/fld.4904